Nano Research

Open Access

Research Article

A robust and frequency-customizable carbon-based electromagnetic wave absorber via solvent-free reversible deactivation radical polymerization strategy

Haoyang Feng[1,§], Qianqian Niu[2,§], Ying Huang[2] ✉, Chen Wang[1], and Zhenhua Wang[1] ✉

[1] *Frontiers Science Center for Flexible Electronics (FSCFE) & Institute of Flexible Electronics (IFE), Northwestern Polytechnical University, Xi'an 710072, China*
[2] *MOE Key Laboratory of Material Physics and Chemistry Under Extraordinary Conditions, School of Chemistry and Chemical Engineering, Northwestern Polytechnical University, Xi'an 710072, China*
[§] *Haoyang Feng and Qianqian Niu contributed equally to this work.*

Cite this article: *Nano Research*, **2026**, *19*, 94908820. https://doi.org/10.26599/NR.2026.94908820

ABSTRACT: Rational designs of electromagnetic (EM) wave absorbers with stable and well-defined chemical structures are crucial for achieving robustness and customization in the EM wave absorption frequency. Herein, we propose a controlled chemical synthesis method for well-defined fluorinated polymer modified graphene nanosheets. The minimum reflection loss frequency of modified graphene can be robustly adjusted from the high-frequency band to low frequency by altering the number of fluorine atoms. Notably, this strategy achieves up to 99.9% reflection loss across S, C, X, and Ku bands, enabling broadband EM wave absorption from 3.47 to 17.51 GHz through the modified graphene compound. Experimental results and theoretical modeling further reveal that the degree of polymer fluorination exhibits a clear positive correlation with the proportion of polarization loss in the low-frequency band. This work demonstrates a powerful chemical control method, offering a promising strategy for designing frequency-customizable EM wave absorbers with wide absorption bandwidths and well-defined structures.

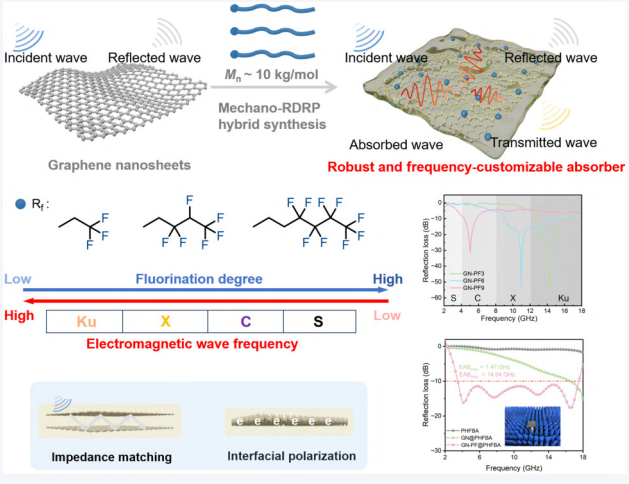

KEYWORDS: mechanochemistry, reversible deactivation radical polymerization, graphene, fluorinated polymer, electromagnetic wave absorption

1 Introduction

Graphene manifests a highly ordered two-dimensional monolayer structure composed of hexagonal carbon atoms, characterized by low apparent density and exceptional electrical conductivity [1–3]. Theoretically, it can efficiently convert electromagnetic (EM) wave into electrical energy and dissipate it. In practical applications, the EM wave attenuation of graphene is constrained by high electromagnetic parameters and frequency dispersion, hindering substantial breakthroughs in the absorption of multi-band EM wave [4–6]. Currently, various methods have been developed for fabricating graphene-based absorbers targeting multi-band EM wave absorption, including complex micro/nano structures [7–11], carbon-magnetic composites [12–14], edge modifications [15–17], and heteroatom defect engineering [18, 19]. These strategies artificially introduce defects into graphene structures to alter the bandgap configuration, thereby adjusting the dielectric constant to achieve impedance matching [20, 21]. They also incorporate multiple loss mechanisms to broaden the effective absorptive bandwidth. However, in the application of absorbers, the robustness and tunability of their EM wave absorption frequency bands remain challenging. Due to the introduction of complex porous structure, nanoparticles, and impurity atoms, the intrinsic chemical inertness of graphene is compromised. Undesirable

Received: March 18, 2026; **Revised:** April 19, 2026
Accepted: May 8, 2026

✉Address correspondence to Ying Huang, yingh@nwpu.edu.cn; Zhenhua Wang, iamzhwang@nwpu.edu.cn

adsorption effects [22], catalytic effects [23], and chemical reactivity [24] often lead to unpredictable shifts in EM wave absorption performance. Therefore, one key strategy is to develop a novel approach for synthesizing chemically inert and structurally stable carbon-based EM wave absorbers whose absorption bands can be easily tuned and are not compromised by common chemical reaction conditions.

Fluorinated and semi-fluorinated polymers with intrinsic low surface energy exemplify stable and durable macromolecular systems [25, 26]. Fluorinated materials often exhibit superior thermal stability, chemical stability, and electrochemical stability relative to hydrogenous analogues [27, 28]. They are therefore attractive materials for extensive applications in protective coatings, sealing gaskets, printed circuit boards, and lithium-ion batteries [29]. Fluorinated polymer modified graphene effectively reduces the overall surface energy of absorber powders, enhancing their environmental stability and electromagnetic field durability. Due to their inherently low dielectric constant, fluorinated polymers typically exhibit complete EM wave transmission characteristics, rendering them nearly transparent to microwaves [30]. Reported fluorinated polymer carbon-based composites commonly serve as primary contributors in electromagnetic shielding applications [31–33]. We observe that fluorides can promote the separation of specific functional groups toward interfaces with low dielectric constants (such as air or vacuum), enabling the modification of its electromagnetic parameters through chemical structure regulation [34]. Given that the chemical structure of polymers is jointly determined by the chemical structure of monomers and the macromolecular chain structure, it is crucial to develop synthetic techniques for preparing fluorinated polymers with defined structures for investigating the electromagnetic properties of fluorinated polymer modified graphene.

Reversible deactivation radical polymerization (RDRP) stands as one of the most powerful methods for synthesizing polymerization product with predetermined molecular weights, narrow molecular weight distributions, and excellent chain-end fidelity [35–38]. Given the excellent properties and practical application value of fluorinated polymers, researchers have developed various synthetic techniques for preparing fluorinated polymers with well-defined structures through the polymerization of fluorinated or semi-fluorinated monomers [39–42]. However, these existing methods typically rely on special solvents or metal catalysts, making them unsuitable for the hybrid synthesis of absorbers [43, 44]. In this work, we report a fluorinated polymer modified graphene with a well-defined structure (polymer number-average molecular weight M_n ~ 10 kg/mol), which can be controllably synthesized via a solvent-free mechanochemical RDRP hybrid synthesis. This absorber consists of a fluorinated polymer surface and a graphene core, forming a uniform graphene distribution and abundant heterointerfaces. By altering the chemical structure of fluorinated polymer, the form of EM wave loss and dissipation capacity can be adjusted, enabling EM wave absorption to be tuned between the Ku, X, C, and S bands (Fig. 1). The fundamental nature of polymer chemistry provides a new paradigm for EM wave absorption and offers a promising macromolecular design strategy for developing absorbers with customizable frequency bands.

2 Experimental

2.1 Main materials

Graphene nanosheets (GN) were purchased from Cabot (USA). 2,2,2-Trifluoroethyl acrylate (TFEA), 2,2,3,4,4,4-hexafluorobutyl acrylate (HFBA), 2-(perfluorobutyl) ethyl acrylate (NFHA), dibenzoyl peroxide (BPO), and ethylene diacrylate were all purchased from Adamas-beta® (China). Triethylborane/4-methoxypyridine complex initiator (Et_3B-PyOMe) and 2-(dodecylsulfanylthiocarbonylsulfanyl)-2-methylpropionic acid (DDMAT) were synthesized according to the method in our past article [37]. All monomers were purified by passing through basic alumina, and other materials were used without further treatment.

2.2 Synthesis of fluorinated polymer modified graphene

For GN-PF3, in 5 mL stainless steel jar equipped with six 4 mm balls, 0.2 mL (1.58 mM, 200 equiv.) TFEA monomer, 2.9 mg (0.008 mM, 1 equiv.) DDMAT, 16.3 mg (0.08 mM, 10 equiv.) Et_3B-PyOMe, and 194.6 mg (80 wt.% monomer) graphene nanosheets were mixed. The final reaction mixtures were ball-milled under air at 25 Hz for 1 h to obtain the GN-PF3. The polymer for testing was obtained by sonicating hybrid graphene in solution for 30 min. Modified graphene was prepared using HFBA and NFHA monomers, respectively, and named GN-PF6 and GN-PF9.

2.3 Synthesis of GN-PF@PHFBA composites

Modified graphene (GN-PF3/GN-PF6/GN-PF9), HFBA, ethylene diacrylate, and BPO in a mass ratio of 20(8:4:8):80:1:0.2 were mixed and cured at 60 °C for 24 h to obtain GN-PF@PHFBA composites.

3 Results and discussion

3.1 Synthesis of well-defined fluorinated polymer modified graphene via solvent-free mechanochemical methods

Semi-fluorinated acrylic esters are commercially available liquid

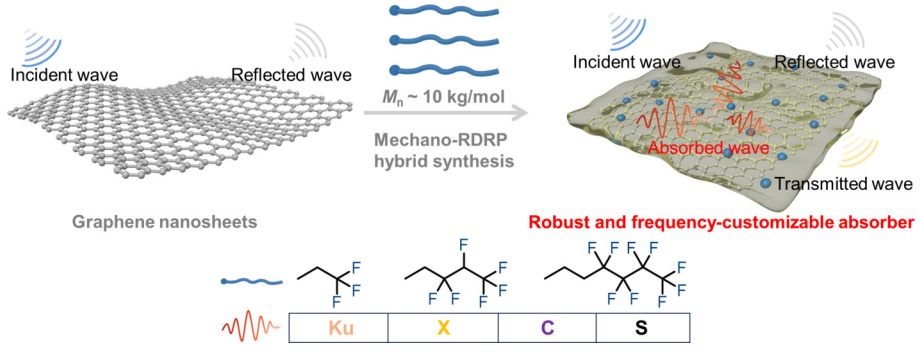

Figure 1 Schematic diagram of the preparation of a robust and frequency-customizable EM wave absorber via solvent-free mechanochemical RDRP hybrid synthesis.

fluorinated monomers featuring side chains with customizable fluorine atom counts [45]. The synthesized polymers exhibit the superior properties of fluorinated polymers (stability and low dielectric constant). The synthesis of fluorinated polymer modified graphene utilizes partially fluorinated acrylic acid esters as a shell layer to adjust the dielectric constant and impedance matching of pristine graphene nanosheets. Furthermore, the known effects of M_n and molecular weight distribution (M_W/M_n) on altering the fundamental properties of the polymer are explored. Therefore, we developed a solvent-free mechano-RDRP hybrid synthesis to generate target polymer modified graphene with predefined chain lengths (Scheme S1 in the Electronic Supplementary Material (ESM)) [37]. To investigate the influence of fluorinated polymer type, we synthesized fluorinated polymer modified graphene with identical M_n and narrow molecular weight distribution (M_W/M_n < 1.2) using semi-fluorinated acrylic ester monomers containing different numbers of fluorine atoms (TFEA, HFBA, and NFHA) (Tables S1 and S2 and Figs. S1–S9 in the ESM), named GN-PF3, GN-PF6, and GN-PF9, respectively.

The intrinsic high surface energy of graphene nanosheets is incompatible with the low surface energy of semi-fluorinated monomers, which significantly limits the conventional solvent-based synthesis of fluorinated polymer modified graphite [46]. In this work, we innovatively employed a solvent-free mechanochemical approach to overcome the substantial surface energy disparity. Due to its highest fluorine atom content, NFHA monomer exhibits an even more pronounced surface energy difference compared to graphene nanosheets. To clarify the effective hybrid formation between fluorinated polymers and graphene, we first analyzed the surface morphology and elemental composition of GN-PF9 using scanning electron microscopy (SEM), transmission electron microscopy (TEM), and energy-dispersive spectroscopy (EDS). SEM images reveal that the GN-PF9 exhibits a well-ordered layered morphology consistent with the pristine graphene nanosheet morphology, indicating that the mechanochemical hybrid process has scarcely altered the original graphene nanosheet's structural features (Fig. 2(a) and Fig. S10 in the ESM). Further observation using TEM revealed opaque regions between graphene layers, which may be attributed to the insulating fluorinated polymer blocking electron transport (Fig. 2(b) and Fig. S11 in the ESM). Based on this hypothesis, we analyzed the surface elemental composition of this region via EDS. The results indicated that the opaque regions correspond to significant fluorine element aggregation (Figs. 2(c) and 2(d)). Additionally, we employed SEM and EDS to analyze the surface morphology and elemental composition of both the raw graphene nanosheets after ball milling and all GN-PF samples. The results indicate that ball milling of pristine graphene nanosheets generates graphene fragments, severely disrupting the morphology of the nanosheets (Fig. S12 in the ESM). In contrast, GN-PF prepared via a mechano-RDRP hybrid approach exhibits a well-ordered layered structure, with morphology largely consistent with that of pristine graphene nanosheets (Figs. S13–S15 in the ESM). Elemental analysis results indicate that GN-PF samples exhibit distinct fluorine element contrast compared to the original graphene nanosheets subjected to ball milling treatment. Semi-quantitative elemental composition analysis at randomly selected points revealed a gradient increase in fluorine content for GN-PF3, GN-PF6, and GN-PF9, confirming the feasibility of mechano-RDRP for hybrid-regulated modification of surface fluorine content in graphene (Fig. S16 in the ESM). These results demonstrate that despite substantial surface energy differences, semi-fluorinated monomers can effectively coat graphene nanosheets with minimal impairment to their surface morphology during *in-situ* polymerization hybridization.

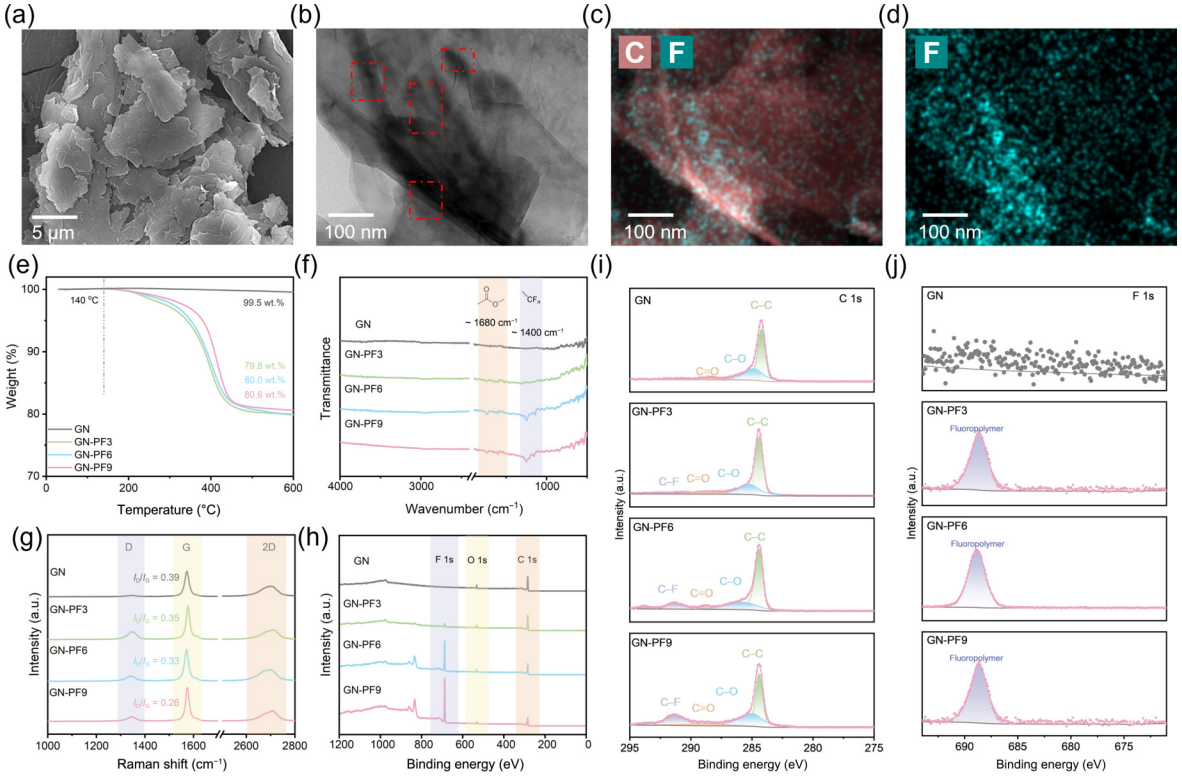

Figure 2 (a) SEM image, (b) TEM image, and ((c) and (d)) EDS elemental mapping of GN-PF9 sample. (e) TGA curves, (f) FTIR spectra, (g) Raman spectra, (h) XPS spectra, (i) high-resolution C 1s XPS spectra, and (j) high-resolution F 1s XPS spectra of GN and GN-PF samples.

To eliminate the influence of fluorinated polymer mass fraction on fluorine content of GN-PF samples, we characterized the fluorinated polymer mass fraction of each GN-PF sample using thermogravimetric analysis (TGA) under an inert gas atmosphere (Fig. 2(e)). As a control, pristine graphene nanosheets exhibited thermal stability up to 600 °C. The thermal degradation curves of all GN-PF samples showed no significant decline before 140 °C, indicating negligible residual monomers in the modified samples [47]. Ultimately, the residual weights of all modified graphene groups at 600 °C were around 80 wt.%, suggesting comparable polymer contents across different samples. These results demonstrate that the solvent-free mechano-RDRP hybrid synthesis achieves significantly higher synthesis efficiency than solvent-based approaches by controlling polymer mass fraction through feed ratio regulation.

During the synthesis process, we have confirmed the chemical structure of the polymer via hydrogen nuclear magnetic resonance (^{1}H NMR) spectroscopy (Figs. S2–S7 in the ESM). As a supplement, we employed Fourier transform infrared spectroscopy (FTIR) to confirm the functional group composition of the GN-PF samples. Figure 2(f) displays the infrared absorption peaks of the pristine GN and GN-PF samples. Due to its strong absorptive properties, pristine GN sample exhibits almost no characteristic peak patterns. The pronounced absorption peak at 1400 cm^{-1} in the GN-PF samples is typically attributed to the stretching vibration of fluorinated groups. Additionally, a characteristic absorption peak for acrylic polymer was observed near 1680 cm^{-1}. Furthermore, we employed Raman spectroscopy to characterize the degree of graphitization and the transition of ordered structures in the GN-PF samples (Fig. 2(g)). In Raman spectra of carbon material, the D peak typically represents disordered carbon structures within the sample, while the G peak corresponds to graphite structures [24]. Raman spectra exhibit that the integral ratio of D peak to G peak (I_D/I_G) for pristine GN is 0.39, while the I_D/I_G values for the GN-PF samples are 0.35, 0.33, and 0.26, respectively. Furthermore, the 2D peak of each modified graphene sample exhibits significant broadening and a multi-peak morphology. These results indicate active radicals generated by mechanical force deliberately attack defect sites or edges to generate active carbon radicals, which simultaneously initiate the polymerization and fix defects. We also used X-ray photoelectron spectroscopy (XPS) to determine the valence states of surface elements in the modified graphene samples (Fig. 2(h)) [28]. The rough scanning spectrum indicates that the fluorine content corresponds to the chemical structure of the GN-PF samples. To elucidate the chemical bonding of elements in detail, we performed peak shape fitting analysis for the major carbon, oxygen, and fluorine elements (Figs. 2(i) and 2(j) and Fig. S17 in the ESM). The high-resolution C 1s spectrum of pristine graphene decomposes into peaks at 284.6 eV (C–C), 285.7 eV (C–O), and 288.4 eV (C=O), indicating residual oxides remain in the pristine GN. Unlike pristine GN, the GN-PF samples exhibit distinct fluorine peaks. Fitting analysis reveals only one major peak at 688.2 eV, indicating that the fluorine atoms are chemically bonded in a single configuration and originate solely from the solvent-free hybrid reaction.

3.2 Frequency-customizable EM wave absorption properties and mechanism analysis

Carbon-based absorbers typically exhibit effective absorption bandwidths (EAB) in the high frequency region [48]. However, most of the microwave application scenarios operate within the relatively low frequency range of less than 10 GHz, which significantly limits the practical value of carbon-based absorbers [6]. We addressed this limitation by preparing modified graphene nanosheets with surfaces of various fluorinated polymers using a solvent-free mechano-RDRP hybrid method. First, the coaxial method was employed to evaluate the influence of GN-PF samples with different chemical structures on the EM wave absorption. Figure 3(a) displays 2D contour diagrams of reflection loss (RL) values versus frequency at different thicknesses of the pristine GN samples. Constrained by its inherently high dielectric constant, pristine GN sample reflects a significant portion of EM waves, exhibiting virtually no effective EM wave absorption band (RL_{min} > −10 dB, Figs. S18(a) and S19(a) in the ESM). Figures 3(b)–3(d) and Figs. S18 and S19 in the ESM show the effective EM wave absorption bands of GN-PF samples modified with different fluorinated polymers at various thicknesses. The GN-PF6 sample, featuring moderate polymer fluorine content, exhibits the optimal effective absorption bandwidth (EAB_{max} = 7.08 GHz within the 10.92–18.00 GHz frequency range). To achieve superior absorptive performance, we prepared GN-PF6 samples with loading levels of 10 wt.%, 20 wt.%, and 30 wt.% (designated as GN-PF6-10, GN-PF6-20, and GN-PF6-30, respectively) and tested their electromagnetic parameters. The results indicate that both increasing and decreasing the loading amount leads to a decrease in EAB_{max} (Fig. S20 in the ESM). Specifically, the EAB_{max} for the GN-PF6-10 specimen was 5.81 GHz, while that for the GN-PF6-30 specimen was 4.86 GHz (Fig. S21 in the ESM). To clarify the cause of this trend, we further analyzed the electromagnetic parameters of samples with different loading amounts. Results indicate that as loading increases, the complex permittivity (ε' and ε'') significantly rises, and the Cole–Cole curve exhibits more linear segments (conductive loss) rather than a regular semicircle (polarization loss) (Figs. S22 and S23 in the ESM). In addition, the GN-PF6-10 sample with low loading amount demonstrated superior reflection loss performance (RL_{min} = −58.79 dB). These findings suggest that excessive loading may induce the formation of conductive pathways, thereby compromising the insulating properties of the fluorinated polymer shell [30].

Importantly, the reflection loss performance of GN-PF samples with different fluorine contents exhibits distinct regularities. To observe this pattern more clearly, we compared the EM wave frequency bands corresponding to the RL_{min} values of different samples. As shown in the Fig. 3(e), with the increase in the fluorine atoms of the semi-fluorinated acrylic esters, the RL_{min} of the GN-PF samples shifts toward lower frequencies (from 14.24 to 5.04 GHz). Since the EAB_{max} of the various GN-PF samples vary significantly, we first analyze the impact of the loading impedance on the absorption frequency range.

It is well known that a sample acting as a load exhibits a unique characteristic impedance during the propagation of EM waves through a waveguide cavity. Unless this characteristic impedance matches that of free space (377.3 Ω), the EM wave will be reflected and superimposed with the incident wave, forming a standing wave [49]. As a representative technique in the field of electronics, the Smith chart method has long been employed to evaluate impedance matching performance [50]. By analyzing the trace lines on the Smith chart, we can rapidly determine whether the free-space impedance of an EM wave absorber reaches the gray circle region at the chart's center (perfect absorption). The trace line for GN-PF

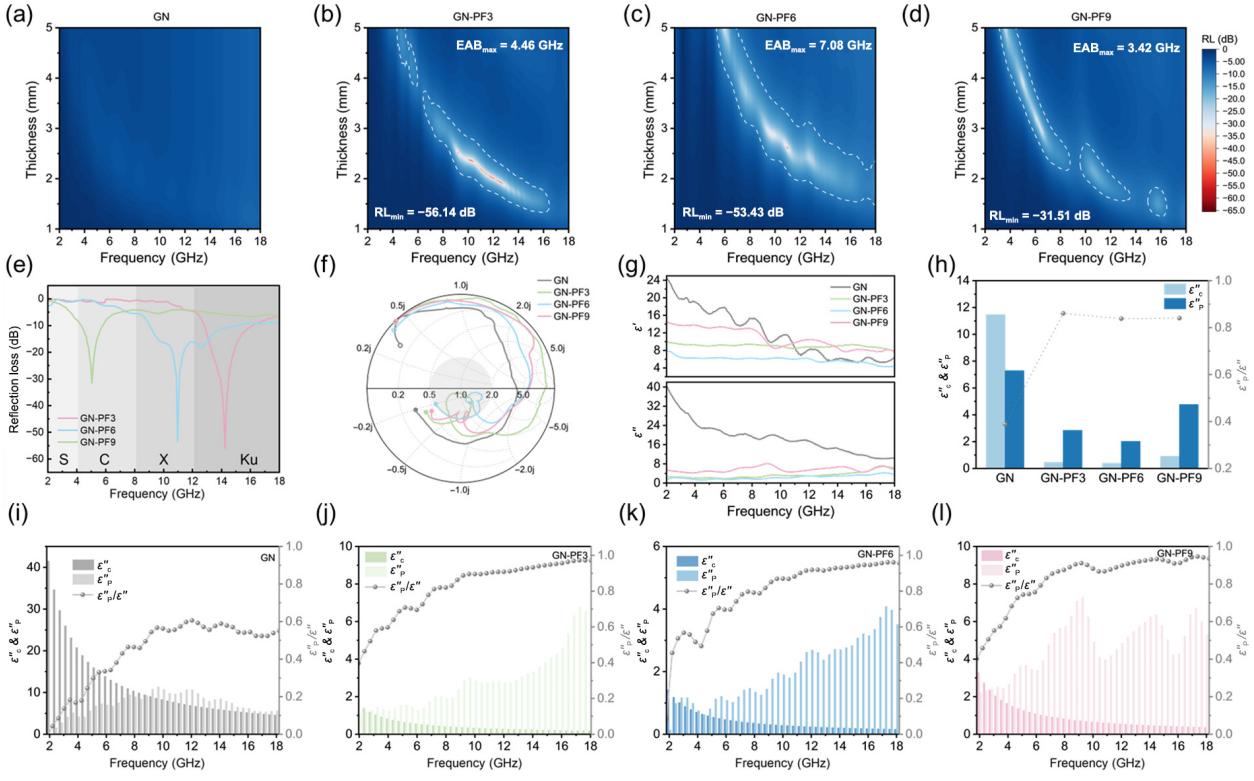

Figure 3 2D curves of RL values versus frequency at different thicknesses: (a) GN, (b) GN-PF3, (c) GN-PF6, and (d) GN-PF9 samples. (e) Comparison of the minimum RL curves for different samples. (f) Smith charts of GN and GN-PF samples with frequency markers (hollow circles: 2 GHz; solid circles: 18 GHz). Gray-shaded region denotes the fluctuation range around the ideal normalized impedance ($|Z| = 1$), reflecting tolerance thresholds for effective impedance matching. (g) Complex permittivity of GN and GN-PF samples in 2–18 GHz band. ε': real part, ε'': imaginary part. (h) Conduction loss (ε''_c), polarization loss (ε''_p), and the ratio of polarization loss ($\varepsilon''_p/\varepsilon''$) of the GN and GN-PF samples. (i)–(l) Comparison of ε''_c, ε''_p, and $\varepsilon''_p/\varepsilon''$ for GN and GN-PF samples at 2–18 GHz.

samples approaches the chart's center (0.5–2.0), indicating ideal impedance matching (Fig. 3(f)). In contrast, the trace line for pristine GN sample remains distant from the gray circle region. We also calculated the impedance matching values Z ($Z = Z_{in}/Z_0$, Z_{in}: input impedance of the sample; Z_0: impedance of free space) for each group of samples (Fig. S24 in the ESM). As a reference, the Z values of the GN samples remained below 0.4 across the entire 2–18 GHz frequency band for thicknesses ranging from 1 to 5 mm, exhibiting the poorest impedance matching characteristics. GN-PF3 with the lowest fluorine content exhibits optimal impedance matching characteristics, approaching the ideal free-space Z value (1.0) in the low frequency region. Surprisingly, all GN-PF samples demonstrate favorable impedance matching properties at low frequency region rather than high frequency region. Additionally, an ideal EM wave absorber should exhibit excellent impedance matching and highly efficient EM wave attenuation capabilities. We also calculated the attenuation coefficient α ($\alpha = \tan\varepsilon'/\varepsilon'$) to evaluate the EM wave attenuation performance of the modified graphene. All GN-PF absorbers exhibited high attenuation constants exceeding 100 within the effective absorption band (Fig. S25 in the ESM). The GN-PF9 sample demonstrated significantly higher attenuation constants in the low-frequency range compared to the other two modified graphene samples, attributed to the superior wave-transmitting properties of its fluorinated polymer shell.

To elucidate the intrinsic mechanism behind the frequency-dependent absorption behavior, we analyzed the complex permittivity (ε' and ε'') of each graphene sample as a function of EM wave frequency (Fig. 3(g) and Fig. S26 in the ESM). As shown in Fig. 3(g), both ε' and ε'' of pristine GN samples decrease with increasing EM wave frequency, whereas ε'' of all GN-PF samples exhibits varying degrees of increase with frequency. This result suggests that the insulating fluorinated shell physically modulates the GN–GN contact, transitioning the system from continuous macroscopic currents (high reflection) to micro-capacitor networks (enhanced micro-current conduction loss and hopping electron tunneling effect) [51]. We also plotted Cole–Cole plots to evaluate the dielectric loss behavior of all graphene samples. The results indicate that all Cole–Cole curves of the GN-PF samples comprise regular semicircles (polarization loss) and straight lines (conductive loss) (Fig. S27 in the ESM). Based on the Debye theory, we quantified the polarization loss and conductive loss using electromagnetic parameters [52]. As shown in the Fig. 3(h), analysis of the average polarization loss and conduction loss across the entire 2–18 GHz frequency band for all graphene samples indicates that the polarization loss of GN-PF samples accounts for approximately 0.838–0.861 of the total dielectric loss. In contrast, the polarization loss of pristine GN sample constitutes only 0.388 of the total dielectric loss. We further compared the polarization loss percentage across different frequency bands for GN-PF samples (Figs. 3(i)–3(l)). GN-PF9 sample exhibited the highest polarization loss percentage in the C-band, GN-PF6 sample in the X-band, and GN-PF3 sample in the Ku-band, which aligns perfectly with the optimal reflection loss frequency bands demonstrated by GN-PF samples. In the Maxwell–Wagner model, there is a cascading difference in permittivity: $\varepsilon_{Graphene} > \varepsilon_{Fluoropolymer} > \varepsilon_{Air}$. The polymer creates a gradient impedance bridging layer, yielding enhanced polarization at the GN/Polymer interface compared to a direct, abrupt GN/Air boundary [53, 54]. The above results indicate that

different fluorinated polymers, due to variations in their dielectric constants, provide different polarization intensity at the heterointerface formed with graphene.

In summary, we have prepared modified graphene with well-defined fluorinated polymer shell. The interlayers of modified graphene samples contain fluorinated polymers with customizable chemical structures. These fluorinated polymers exhibit low dielectric constants, enabling excellent impedance matching with free space and enhancing the transmission of electromagnetic waves. Furthermore, polarization loss, as the primary loss mechanism, contributes to the customizable electromagnetic absorption bands of the GN-PF samples (Fig. 4).

3.3 Practical application evaluation of EM wave absorption performance

To comprehensively validate the EM wave performance of GN-PF absorbers in practical applications, we employed CST Studio Suite software to simulate radar cross section (RCS) at specific frequencies [55]. By measuring the intensity of reflected EM waves detected by radar signals at different angles, we characterize an object's "visibility" on radar. Consequently, EM wave absorption rate serves as the core metric for the software's algorithms.

The practical application of the obtained fluorinated polymer modified graphene was further evaluated through RCS values (Fig. 5(a)). Here, we compare the differences in dielectric material properties between samples by examining the 3D far-field radiation patterns and the 2D radar cross-section distributions of a perfect electrical conductor (PEC) plate and a PEC plate covered with absorptive material at different detection angles (Fig. 5(b)). The radar scattering signal intensity of the pristine PEC sheet is quite significant (Fig. 5(c)). As a control, the radar scattering signal intensity of the pristine GN absorbers is similar to that of the PEC substrate, exhibiting negligible radar stealth properties (Fig. 5(d) and Fig. S28 in the ESM). The GN-PF3 absorber exhibited the smallest RCS value within the angle range of $-90° < \theta < 90°$ compared to other samples, indicating that the GN-PF3 absorber can significantly reduce radar scattering intensity. All GN-PF samples exhibit effective RCS value across the entire detection angle range from −90° to 90° (Fig. S28 in the ESM). In addition, the RCS reduction gradually diminishes as the test angle increases, starting from the four selected detection angles (0°, 30°, 60°, and 90°) (Fig. S29 in the ESM). Notably, at a test angle of 24°, the GN-PF6 absorber achieved a minimum RCS value of −42.2 dB, demonstrating significant application potential. These encouraging results indicate that radar scattering intensity can be substantially reduced, and the fluoropolymer coating strategy can be applied to carbon materials to maximize electromagnetic energy dissipation.

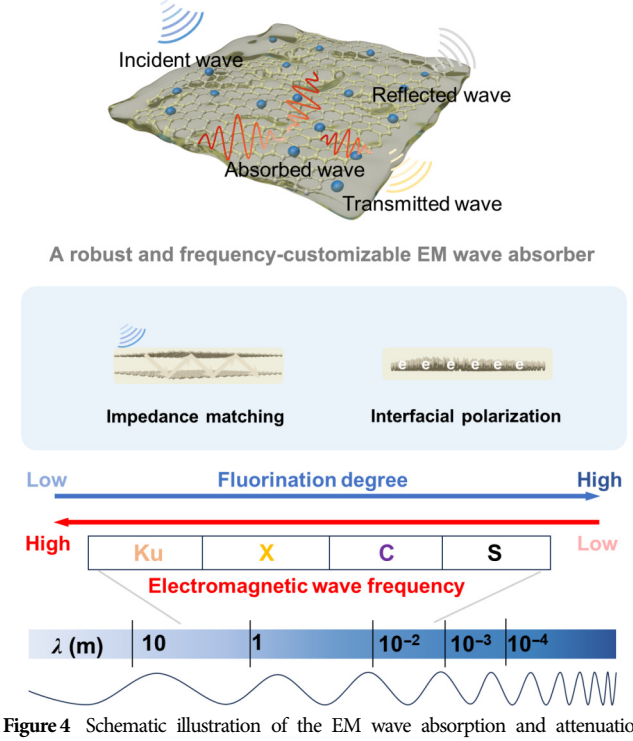

Figure 4 Schematic illustration of the EM wave absorption and attenuation mechanism for GN-PF samples.

Additionally, we utilized CST Studio Suite software to analyze the electric field intensity and power loss density within the fundamental unit cell to validate the attenuation mechanism of the GN-PF absorbers [50]. First, the sample thickness corresponding to the optimal EAB was simulated and calculated. Subsequently, the frequency yielding the highest EM wave absorption rate at this thickness was selected. Simulation results indicate that when vertically incident EM waves pass through the GN-PF absorbers, the electric field distribution undergoes significant changes (Fig. 5(e)), while the magnetic field distribution remains nearly unchanged (Fig. 5(f)). These simulations confirm that the GN-PF absorbers primarily achieve microwave dissipation through dielectric conduction. The study reveals that the simulated power loss density correlates with the attenuation constant, with red regions on the model surface indicating stronger microwave absorption capabilities (Fig. 5(g)). We observe that energy dissipation is predominantly concentrated in the central and upper regions of the modified graphene model, suggesting that the fluorinated polymer layer on the surface of the modified graphene contributes the majority of EM wave dissipation.

3.4 Performance stability evaluation of GN-PF absorbers

The reliability and stability of EM wave absorption performance are crucial dimensions for evaluating EM wave absorbers [51]. However, the impact of conventional processing and fabrication on absorber powders featuring complex micro/nano structures and defect modifications remains an understudied area.

To validate the practicality of the fluorinated polymer modified graphene, we fabricated large-scale structural components and evaluated their mechanical properties, moisture and heat stability, electrochemical stability, anti-soiling performance, and absorptive capabilities (Fig. 6(a)). First, we conducted tensile tests to evaluate the mechanical properties of GN-PF@PHFBA specimen (Fig. 6(b)). The results indicate that GN-PF@PHFBA exhibits superior fracture strength (3.4 MPa) and elongation at break (178%), outperforming both the GN@PHFBA control specimen and the fluorinated polymer PHFBA specimen. Thermogravimetric analysis was conducted on samples that had undergone 48-h humidity-heat treatment and electrolytic cell treatment, respectively (Fig. S30 in the ESM). The results showed that the thermogravimetric curves of the samples subjected to extreme conditions were similar to those of the pristine samples. SEM images of the fracture surfaces reveal that the GN@PHFBA specimen exhibits a highly rough cross-section with multiple defects (Fig. 6(c)). The GN-PF@PHFBA exhibits a smooth and flat cross-section consistent with that of the fluorinated polymer PHFBA specimen (Fig. 6(d) and Fig. S31 in the

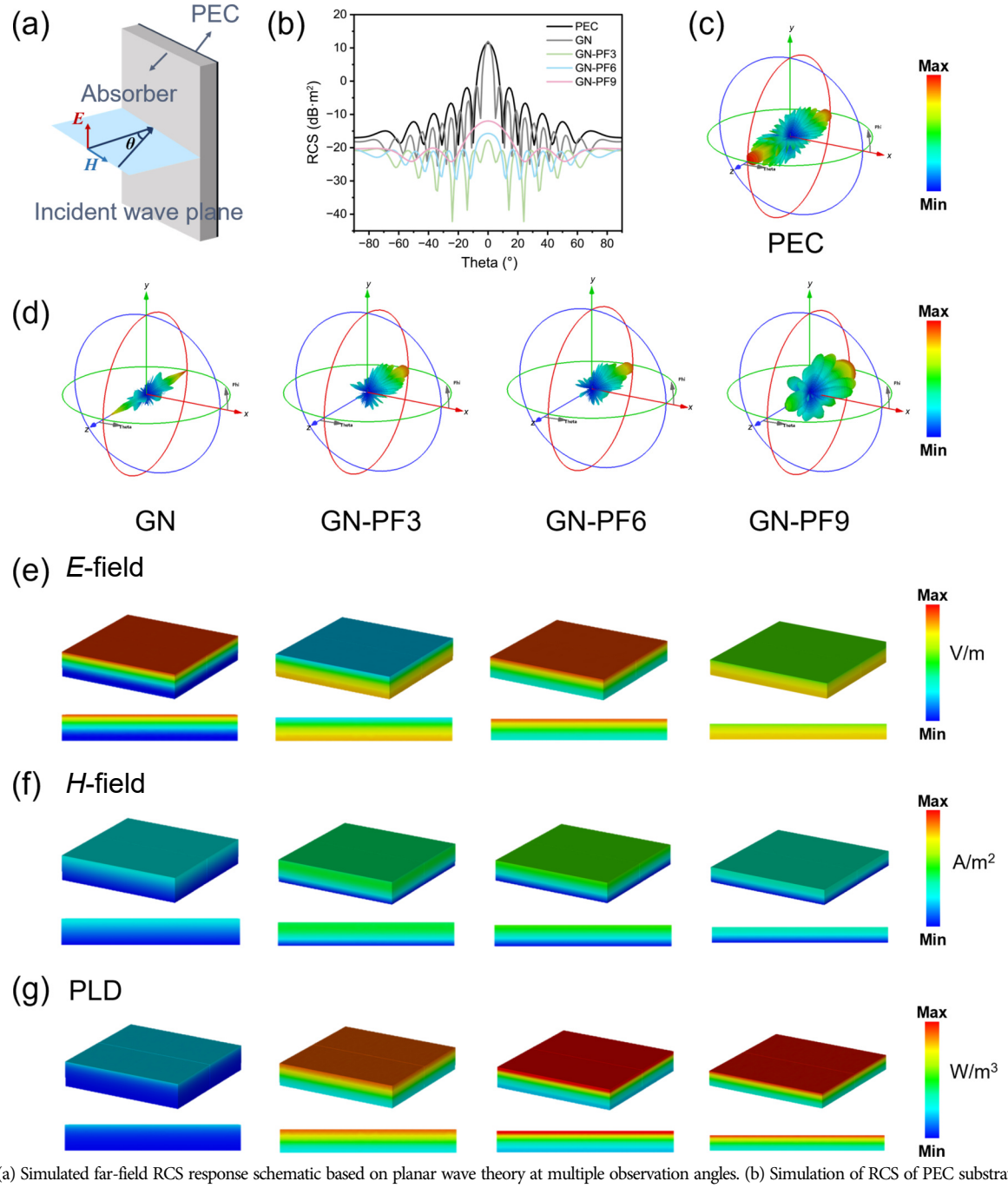

Figure 5 (a) Simulated far-field RCS response schematic based on planar wave theory at multiple observation angles. (b) Simulation of RCS of PEC substrate and PEC substrate with the GN and GN-PF absorbers coating under different scanning angles. (c) and (d) Far-field response based on the plane wave theory of PEC, GN, and GN-PF absorbers. Distributions of the (e) electric field, (f) magnetic field, and (g) power loss density of GN and GN-PF absorbers respectively at 14.24, 10.96, and 5.04 GHz.

ESM). These results indicate that GN-PF samples retain the integrity of their composite structure during the molding process, demonstrating reliable mechanical properties and consistent quality under extreme environmental conditions.

According to the Shuttleworth equation, liquid precursors must overcome substantial surface energy barriers to wet graphene materials, which typically leads to agglomeration of lightweight carbon materials within resin precursors [43]. We employed a solvent-free mechano-RDRP hybrid approach to enrich semi-fluorinated acrylic monomers on graphene surfaces, thereby reducing the surface energy disparity between the two and polymerizing them into fluorinated polymer surfaces. This low-surface-energy fluorinated polymer shell theoretically enhances the wettability of modified graphene by resin precursors. As a validation experiment, we prepared a hydrophobic absorber GN-PF@PHFBA based on the radical curing process of fluorinated acrylate monomers, using unmodified pristine GN as a control. The hydrophobicity is crucial for the durability of coatings, including anti-fouling, de-icing, and salt spray resistance [56]. Therefore, we evaluated the hydrophobicity of each specimen using contact angle measurements (Fig. 6(e)). Benefiting from the inherently low surface energy of fluorinated polymers and the excellent compatibility of modified graphene, GN-PF@PHFBA specimen exhibits outstanding hydrophobicity, with a static water contact

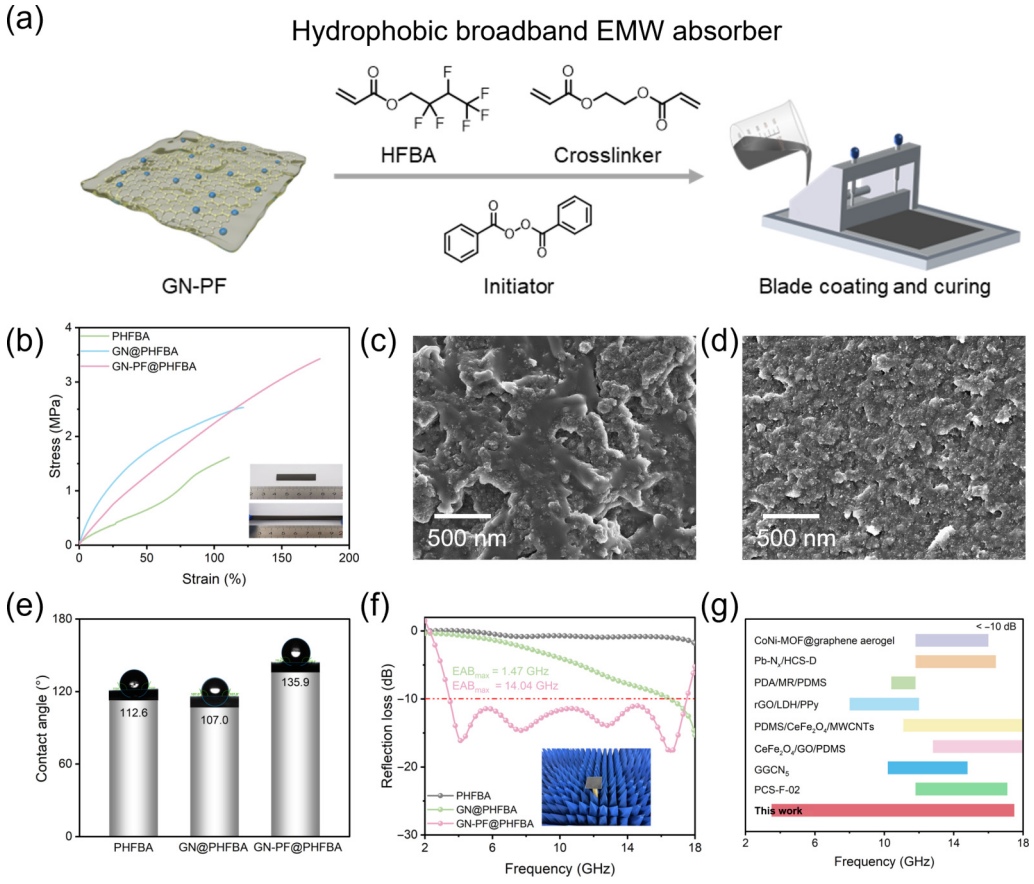

Figure 6 (a) Flowchart for the preparation of hydrophobic broadband EM wave GN-PF@PHFBA absorber. (b) Tensile stress–strain curves of PHFBA, GN@PHFBA, and GN-PF@PHFBA. SEM images of tensile section for (c) GN@PHFBA and (d) GN-PF@PHFBA. (e) Water contact angle of the PHFBA, GN@PHFBA, and GN-PF@PHFBA surface. (f) The absorptive properties of PHFBA, GN@PHFBA, and GN-PF@PHFBA samples measured using the bow-shaped method, with dimensions of 18 cm × 18 cm. (g) Performance comparison with EM wave absorbers from other hybrid/compound methods (the related articles are listed in the ESM).

angle as high as 135.9°, approaching that of superhydrophobic surfaces (~ 150°) [30].

Finally, we attempted to blend three types of modified graphene (GN-PF3/GN-PF6/GN-PF9) with distinct primary absorption bands to achieve broadband EM wave absorption (Fig. 6(f)). Using −10 dB as the evaluation criterion for effective EM wave absorption, the GN-PF@PHFBA coating achieved broadband EM wave absorption across the 3.47–17.51 GHz range with a thickness of 3.2 mm (Fig. S32 in the ESM, 18 cm × 18 cm). In contrast, PHFBA exhibits near-transparency under 2–18 GHz EM wave, and GN@PHFBA coating demonstrates an effective absorption bandwidth of only 1.47 GHz in the high-frequency region. Compared to previously reported carbon-based absorbers, GN-PF@PHFBA achieves an absorption bandwidth up to 14.04 GHz through controlled chemical structural design, without requiring complex nanostructures, macrostructural engineering, defect modification, or carbon-magnetic composites. These results demonstrate that solvent-free mechano-RDRP for hybrid synthesis of fluorinated polymer modified graphene absorbers not only offers simple preparation, chemical stability, and matrix compatibility but also achieves the widest absorption bandwidth based solely on dielectric loss to date (Fig. 6(g)).

4 Conclusion

In summary, semi-fluorinated acrylic monomers form a well-defined fluorinated polymer shell with customizable chemical structure on graphene nanosheets via solution-free mechano-RDRP hybrid synthesis. The surface fluorinated polymer exhibits excellent wave transparency and insulation properties, enabling the absorber to demonstrate favorable impedance matching characteristics in the EM wave frequency band below 10 GHz. In addition, fluorinated polymer shell with precisely customizable fluorine content significantly enhances polarization loss for low-frequency EM waves, achieving customizable EM wave absorption across multiple bands. Through simple compounding, the modified graphene absorber achieves an effective EM wave absorption bandwidth spanning the S/C/X/Ku bands, reaching up to 14.04 GHz. Furthermore, the durability and electrochemical stability of fluorinated polymers substantially enhance the practical application value of graphene absorbers in coatings, elastomers, and structural components. This carbon-based absorber synthesis strategy, based on controlled chemical synthesis, facilitates the establishment of accurate design models linking absorber structure and performance, paving the way for the design of frequency-customizable EM wave absorbers.

Electronic Supplementary Material: Supplementary material (NMR spectra, GPC traces, and preparation reaction formula; SEM images, TEM images, XPS spectra, and other structure characterization results; electromagnetic parameters, EM wave absorption performance data, and simulation calculation results)

is available in the online version of this article at https://doi.org/10.26599/NR.2026.94908820.

Data availability

All data needed to support the conclusions in the paper are presented in the manuscript and the ESM. Additional data related to this paper may be requested from the corresponding author upon request.

Acknowledgements

This work was funded by the National Natural Science Foundation of China (No. 52473009), National Key Laboratory of Aerospace Chemical Power Fund (No. NKLACP420241B20), and State Key Laboratory of Advanced Polymer Materials, Sichuan University (No. sklapm2025-3-13).

Declaration of competing interest

All the contributing authors report no conflict of interests in this work.

Author contribution statement

H. Y. F.: Data curation, project administration, validation, writing manuscript, experimental design. Q. Q. N.: Data curation, project administration, validation, experimental design. C. W.: Partial material characterization. Y. H.: Project administration, funding acquisition. Z. H. W.: Project administration, funding acquisition, writing manuscript. All the authors have approved the final manuscript.

Use of AI statement

None.

References

[1] Kang, G.; Kwon, G.; Jeon, J.; Kwon, J.; Kim, M. K.; Hong, J.; Lee, A. S.; Lee, S.; Lee, B.; Kim, Y. et al. Electromagnetic interference shielding using metal and MXene thin films. *Nature* **2025**, *647*, 356–363.

[2] Park, J. M.; Sun, S. W.; Watanabe, K.; Taniguchi, T.; Jarillo-Herrero, P. Experimental evidence for nodal superconducting gap in moiré graphene. *Science* **2026**, *391*, 79–83.

[3] Voiry, D.; Yang, J.; Kupferberg, J.; Fullon, R.; Lee, C.; Jeong, H. Y.; Shin, H. S.; Chhowalla, M. High-quality graphene via microwave reduction of solution-exfoliated graphene oxide. *Science* **2016**, *353*, 1413–1416.

[4] Li, Y. B.; Shao, H.; Lin, Z. F.; Lu, J.; Liu, L. Y.; Duployer, B.; Persson, P. O. Å.; Eklund, P.; Hultman, L.; Li, M. et al. A general Lewis acidic etching route for preparing MXenes with enhanced electrochemical performance in non-aqueous electrolyte. *Nat. Mater.* **2020**, *19*, 894–899.

[5] Lin, L.; Li, J. Y.; Yuan, Q. G.; Li, Q. C.; Zhang, J. C.; Sun, L. Z.; Rui, D. R.; Chen, Z. L.; Jia, K. C.; Wang, M. Z. et al. Nitrogen cluster doping for high-mobility/conductivity graphene films with millimeter-sized domains. *Sci. Adv.* **2019**, *5*, eaaw8337.

[6] Xiong, X. H.; Zhang, H. B.; Lv, H. L.; Yang, L. T.; Liang, G. S.; Zhang, J. C.; Lai, Y. X.; Cheng, H. W.; Che, R. C. Recent progress in carbon-based materials and loss mechanisms for electromagnetic wave absorption. *Carbon* **2024**, *219*, 118834.

[7] Sheng, J.; Han, Z.; Jia, G. D.; Zhu, S.; Xu, Y. F.; Zhang, X. R.; Yao, Y. X.; Li, Y. Covalently bonded graphene sheets on carbon nanotubes: Direct growth and outstanding properties. *Adv. Funct. Mater.* **2023**, *33*, 2306785.

[8] Wang, Z. C.; Wei, R. B.; Gu, J. W.; Liu, H.; Liu, C. T.; Luo, C. J.; Kong, J.; Shao, Q.; Wang, N.; Guo, Z. H. et al. Ultralight, highly compressible and fire-retardant graphene aerogel with self-adjustable electromagnetic wave absorption. *Carbon* **2018**, *139*, 1126–1135.

[9] Tang, Z. M.; Xu, L.; Xie, C.; Guo, L. R.; Zhang, L. B.; Guo, S. H.; Peng, J. H. Synthesis of $CuCo_2S_4$@Expanded Graphite with crystal/amorphous heterointerface and defects for electromagnetic wave absorption. *Nat. Commun.* **2023**, *14*, 5951.

[10] Zhang, C.; Yang, W.; Jiang, B.; Li, Z. X.; Du, S. X.; Ding, Z. Z.; Wu, X.; Zhu, W. J.; Dong, J. Y.; Kong, L. Y. et al. Structure-driven design of cellular graphene/polystyrene composites with balanced dielectric loss and impedance matching for enabling multiband electromagnetic wave absorption. *Chem. Eng. J.* **2025**, *517*, 164290.

[11] Zhang, C.; Yang, W.; Li, Z. X.; Yang, K.; Kong, L. Y.; Du, S. X.; Dong, J. Y.; Zhu, W. J.; Feng, R. Y.; Ma, Z. H. et al. Enhancing low-frequency electromagnetic wave absorption via induced polarization in honeycomb-structured graphene/polymer flexible fibers. *Chem. Eng. J.* **2026**, *535*, 175183.

[12] Gao, T.; Zhao, R. Z.; Li, Y. X.; Zhu, Z. Y.; Hu, C. L.; Ji, L. Z.; Zhang, J.; Zhang, X. F. Sub-nanometer Fe clusters confined in carbon nanocages for boosting dielectric polarization and broadband electromagnetic wave absorption. *Adv. Funct. Mater.* **2022**, *32*, 2204370.

[13] Qian, Y. T.; Lv, X. W.; Lv, H. L.; Wu, Z. C.; Zhang, H. B.; Liu, M.; Yang, L. T.; Zhao, B.; Luo, K. C.; Zhang, J. C. et al. Controllable synthesis of highly symmetrical streamlined structure for wideband microwave absorption. *Small* **2024**, *20*, 2305625.

[14] Liang, N.; Yin, Z. X.; Guo, J. Y.; Fang, W. Y.; Wang, Q.; Tian, G.; Zhang, D.; Yue, H. J.; Feng, S. H. Yolk–shell structure synergistic defect engineering for boosting electromagnetic wave absorption in Co_9S_8@Humins-derived carbon. *J. Mater. Sci. Technol.* **2023**, *164*, 140–149.

[15] Zhao, B.; Li, R. S.; Men, Q. Q.; Yan, Z. K.; Lv, H. L.; Wu, L.; Che, R. C. Transformation of 2D flakes to 3D hollow bowls: Matthew effect enables defects to prevail in electromagnetic wave absorption of hollow rGO bowls. *Small* **2024**, *20*, 2208135.

[16] Su, Z.; Yi, S.; Zhang, W. Y.; Xu, X. X.; Zhang, Y. Y.; Zhou, S. H.; Niu, B.; Long, D. H. Ultrafine vacancy-rich Nb_2O_5 semiconductors confined in carbon nanosheets boost dielectric polarization for high-attenuation microwave absorption. *Nano-Micro Lett.* **2023**, *15*, 183.

[17] Lv, H. L.; Yao, Y. X.; Li, S. C.; Wu, G. L.; Zhao, B.; Zhou, X. D.; Dupont, R. L.; Kara, U. I.; Zhou, Y. M.; Xi, S. B. et al. Staggered circular nanoporous graphene converts electromagnetic waves into electricity. *Nat. Commun.* **2023**, *14*, 1982.

[18] Tian, S. Y.; Li, A. R.; Cui, J. B.; Sun, Z. H.; Liu, H. S.; Yan, Z. Q.; Ding, H.; Tian, H. S.; Qian, L. Order effect of nitrogen and phosphorus co-doping carbon nanofibers for enhancing electromagnetic wave absorption. *Carbon* **2023**, *203*, 580–589.

[19] Cui, R. P.; Li, Y.; Zhang, X. F.; Duan, Z. W.; Zhao, B.; Wan, C. L. Controlled deintercalation of graphene/organic superlattices with dense atomic-scale steric Schottky heterojunctions for extreme microwave absorption. *Nat. Commun.* **2025**, *16*, 5804.

[20] Jiang, B.; Qi, C. L.; Yang, H.; Wu, X.; Yang, W.; Zhang, C.; Li, S. Y.; Wang, L. H.; Li, Y. F. Recent advances of carbon-based electromagnetic wave absorption materials facing the actual situations. *Carbon* **2023**, *208*, 390–409.

[21] Zhang, C.; Jiang, B.; Wang, C. N.; Yang, W.; Li, Y. F. High yield production of lightweight porous carbon from petroleum coke towards efficient electromagnetic waves absorption in the multi-frequency range. *Carbon* **2025**, *245*, 120844.

[22] Hou, Y. L.; Sheng, Z. Z.; Fu, C.; Kong, J.; Zhang, X. T. Hygroscopic holey graphene aerogel fibers enable highly efficient moisture capture, heat allocation and microwave absorption. *Nat. Commun.* **2022**, *13*, 1227.

[23] Rebarchik, M.; Bhandari, S.; Kropp, T.; Mavrikakis, M. Insights into the oxygen evolution reaction on graphene-based single-atom catalysts from first-principles-informed microkinetic modeling. *ACS Catal.* **2023**, *13*, 5225–5235.
[24] Guo, S.; Garaj, S.; Bianco, A.; Ménard-Moyon, C. Controlling covalent chemistry on graphene oxide. *Nat. Rev. Phys.* **2022**, *4*, 247–262.
[25] Améduri, B.; Boutevin, B.; Kostov, G. Fluoroelastomers: Synthesis, properties and applications. *Prog. Polym. Sci.* **2001**, *26*, 105–187.
[26] Babudri, F.; Farinola, G. M.; Naso, F.; Ragni, R. Fluorinated organic materials for electronic and optoelectronic applications: The role of the fluorine atom. *Chem. Commun*. **2007**, 1003–1022.
[27] Yao, W. Q.; Li, Y. J.; Huang, X. Y. Fluorinated poly(meth)acrylate: Synthesis and properties. *Polymer* **2014**, *55*, 6197–6211.
[28] Kassis, C. M.; Steehler, J. K.; Betts, D. E.; Guan, Z. B.; Romack, T. J.; DeSimone, J. M.; Linton, R. W. XPS studies of fluorinated acrylate polymers and block copolymers with polystyrene. *Macromolecules* **1996**, *29*, 3247–3254.
[29] Ameduri, B. Fluoropolymers: The right material for the right applications. *Chem.—Eur. J.* **2018**, *24*, 18830–18841.
[30] Huang, G.; Shi, R. R.; Sun, J.; Fang, Q. Fluorinated intrinsic low-*k* materials at high frequency with good dielectric performance and excellent hydrophobicity. *Eur. Polym. J.* **2023**, *196*, 112310.
[31] Ma, X. H.; Shen, B.; Zhang, L. H.; Liu, Y. F.; Zhai, W. T.; Zheng, W. G. Porous superhydrophobic polymer/carbon composites for lightweight and self-cleaning EMI shielding application. *Compos. Sci. Technol.* **2018**, *158*, 86–93.
[32] Saha, S.; Chakraborty, T.; Saha, A.; Das, S.; Pramanik, G.; Pradhan, A. K.; Chakraborty, C.; Das, S.; Sutradhar, S. A multi-layer design of hexaferrite decorated graphene derivatives incorporated PVDF nanocomposite films; understanding the role of GO/rGO for outstanding electromagnetic wave absorption at microwave frequencies. *Carbon* **2024**, *220*, 118829.
[33] Abbasi, H.; Antunes, M.; Velasco, J. I. Recent advances in carbon-based polymer nanocomposites for electromagnetic interference shielding. *Prog. Mater. Sci.* **2019**, *103*, 319–373.
[34] Gou, Z. X.; Xi, W. B.; Jiang, W.; Zhang, Z. K.; Zhao, J. P.; Zhou, J.; Su, Y. Study on the dielectric properties of fluorinated graphene. *FlatChem* **2025**, *51*, 100862.
[35] Patten, T. E.; Xia, J. H.; Abernathy, T.; Matyjaszewski, K. Polymers with very low polydispersities from atom transfer radical polymerization. *Science* **1996**, *272*, 866–868.
[36] Wang, J. S.; Matyjaszewski, K. Controlled/"living" radical polymerization. Atom transfer radical polymerization in the presence of transition-metal complexes. *J. Am. Chem. Soc.* **1995**, *117*, 5614–5615.
[37] Feng, H. Y.; Chen, Z.; Li, L.; Shao, X. Y.; Fan, W. R.; Wang, C.; Song, L.; Matyjaszewski, K.; Pan, X. C.; Wang, Z. H. Aerobic mechanochemical reversible-deactivation radical polymerization. *Nat. Commun.* **2024**, *15*, 6179.
[38] Braunecker, W. A.; Matyjaszewski, K. Controlled/living radical polymerization: Features, developments, and perspectives. *Prog. Polym. Sci.* **2007**, *32*, 93–146.
[39] Discekici, E. H.; Anastasaki, A.; Kaminker, R.; Willenbacher, J.; Truong, N. P.; Fleischmann, C.; Oschmann, B.; Lunn, D. J.; Read de Alaniz, J.; Davis, T. P. et al. Light-mediated atom transfer radical polymerization of semi-fluorinated (meth)acrylates: Facile access to functional materials. *J. Am. Chem. Soc.* **2017**, *139*, 5939–5945.
[40] Gong, H. H.; Gu, Y.; Zhao, Y. C.; Quan, Q. Z.; Han, S. T.; Chen, M. Precise synthesis of ultra-high-molecular-weight fluoropolymers enabled by chain-transfer-agent differentiation under visible-light irradiation. *Angew. Chem., Int. Ed.* **2020**, *59*, 919–927.
[41] Hansen, N. M. L.; Jankova, K.; Hvilsted, S. Fluoropolymer materials and architectures prepared by controlled radical polymerizations. *Eur. Polym. J.* **2007**, *43*, 255–293.
[42] Zhao, Y. C.; Chen, Y. F.; Zhou, H. Y.; Zhou, Y.; Chen, K. X.; Gu, Y.; Chen, M. Controlled radical copolymerization of fluoroalkenes by using light-driven redox-relay catalysis. *Nat. Synth.* **2023**, *2*, 653–662.
[43] Han, S. T.; Wen, P.; Wang, H. J.; Zhou, Y.; Gu, Y.; Zhang, L.; Shao-Horn, Y.; Lin, X. R.; Chen, M. Sequencing polymers to enable solid-state lithium batteries. *Nat. Mater.* **2023**, *22*, 1515–1522.
[44] Ren, Z. Y.; Mei, P.; Wang, C. Y.; Chen, D.; Zhang, L.; Zhang, W.; Wang, Z.; Zhang, Z. B. Mechanochemical reversible complexation mediated polymerization enabled synthesis of fluorinated polyacrylate copolymers for room temperature solid-state lithium batteries. *Macromolecules* **2025**, *58*, 3199–3207.
[45] Patil, Y.; Ameduri, B. First RAFT/MADIX radical copolymerization of tert-butyl 2-trifluoromethacrylate with vinylidene fluoride controlled by xanthate. *Polym. Chem.* **2013**, *4*, 2783–2799.
[46] Wu, B. F.; Li, J. R.; Han, S. T.; Mao, J. Y.; Wen, P.; Chen, M.; Zhao, Y. C.; Lin, J.; Lin, X. R. *In-situ* synthesis of fluoropolymer-grafted nanohybrid electrolyte as ion reservoir for Li-metal batteries. *Giant* **2023**, *16*, 100201.
[47] Zhang, Y. Q.; Tamijani, A. A.; Taylor, M. E.; Zhi, B.; Haynes, C. L.; Mason, S. E.; Hamers, R. J. Molecular surface functionalization of carbon materials via radical-induced grafting of terminal alkenes. *J. Am. Chem. Soc.* **2019**, *141*, 8277–8288.
[48] Lin, J. P.; Wang, L. C.; Chu, W. Q.; Yu, H. J.; Chen, Z. P.; Chen, M. J.; Song, W. L.; Gu, X.; Liu, J. R.; Wu, N. et al. Ultrabroadband low-frequency microwave absorption in multiscale aerogel-metamaterial hybrids. *Adv. Funct. Mater.* **2026**, *36*, e27401.
[49] Zhang, Z. W.; Li, Z.; Xia, L.; Wang, R. F.; Cao, Y. S.; Cheng, Z.; Huang, Y. Much enhanced electromagnetic wave absorbing properties from the synergistic effect of graphene/γ-graphyne heterostructure in both gigahertz and terahertz band ranges. *Nano Res*. **2023**, *16*, 88–100.
[50] Qu, N.; Sun, H. X.; Sun, Y. Y.; He, M. K.; Xing, R. Z.; Gu, J. W.; Kong, J. 2D/2D coupled MOF/Fe composite metamaterials enable robust ultra-broadband microwave absorption. *Nat. Commun.* **2024**, *15*, 5642.
[51] Deng, L. C.; Yang, K.; Wang, W. Z.; Zhang, W. J.; Li, Y.; Nan, H. Y.; Chai, X.; Luo, F.; Wu, H. J.; Chen, Q. Ag-doped PDA interface strategy for selective electron transition integrating EMI shielding and anti-corrosion performance. *J. Mater. Sci. Technol.* **2025**, *224*, 292–301.
[52] Niu, Q. Q.; Huang, Y.; Huang, H. J.; Zong, M. A flexible and repairable ultra-broadband electromagnetic wave absorber by liquid–liquid phase separation strategy. *Adv. Mater.* **2025**, *37*, e10139.
[53] Wen, J. M.; Deng, L. C.; Shen, H.; Chen, Q.; Wu, H. J. Plasma-assisted bipolarity carrier modulation in TMDs to accelerate dipole polarization for enhanced electromagnetic attenuation. *Adv. Funct. Mater.* **2026**, *36*, e19086.
[54] Deng, L. C.; Zhang, Y. H.; Xu, H. L.; Zhang, W. J.; Hui, S. C.; Yan, W. X.; Luo, F.; Wu, H. J.; Colombo, P.; Chen, Q. Wearable fabrics against ultra-broadband electromagnetic interference. *Matter* **2026**, *9*, 102697.
[55] Zhao, Z. H.; Zhang, L. M.; Wu, H. J. Hydro/organo/ionogels: "Controllable" electromagnetic wave absorbers. *Adv. Mater.* **2022**, *34*, 2205376.
[56] Patil, Y.; Ameduri, B. Advances in the (co)polymerization of alkyl 2-trifluoromethacrylates and 2-(trifluoromethyl)acrylic acid. *Prog. Polym. Sci.* **2013**, *38*, 703–739.